Carbon 119 (2017) 355–364

Contents lists available at ScienceDirect

Carbon

journal homepage: www.elsevier.com/locate/carbon

Nanohole-structured, iron oxide-decorated and gelatin-functionalized graphene for high rate and high capacity Li-Ion anode

Si-Hwa Lee [a], Moumita Kotal [a], Jung-Hwan Oh [a], Palanichamy Sennu [b], Sung-Ho Park [b], Yun-Sung Lee [b], Il-Kwon Oh [a, *]

[a] Creative Research Initiative Center for Functionally Antagonistic Nano-Engineering, Department of Mechanical Engineering, School of Mechanical and Aerospace Engineering, Korea Advanced Institute of Science and Technology (KAIST), 291 Daehak-ro, Yuseong-gu, Daejeon 34141, Republic of Korea
[b] Faculty of Applied Chemical Engineering, Chonnam National University, 77 Yongbong- ro, Buk-gu, Gwangju 500-757, Republic of Korea

ARTICLE INFO

Article history:
Received 9 February 2017
Received in revised form
11 April 2017
Accepted 17 April 2017
Available online 25 April 2017

ABSTRACT

Graphene hybrid nanostructures have emerged as potential candidates as efficient anode materials for lithium-ion batteries. However, two-dimensional plate-like structures protect rapid transport of lithium ions through the thickness direction, resulting in a long pathway of lithium ions and low rate performances. Here, we report a nanohole-structured, iron oxide-decorated and gelatin-functionalized graphene (D-N-GG) for high rate and high capacity lithium-ion anode. Initially, to produce effective path way of lithium ions, physical nanoholes on the graphene layers were generated by microwave-irradiated iron nanoparticles. And then, the gelatin was used to form nitrogen-doped graphene having more active sites for lithium ion storage. Finally, D-N-GG was synthesized by two-step microwave irradiations shows a three-dimensional interconnected mesoporous structure with a uniform decoration of iron oxide nanoparticles on the nanohole-structured graphene, resulting in highly conductive networks and short diffusion lengths for effective lithium ion transport. As a result, the obtained D-N-GG nanostructure delivered a reversible capacity of 924 mAh g^{-1} even over 40 cycles along with a coulombic efficiency in excess of 99%. Especially, even after 65 cycles with variable current density of 100–800 mA g^{-1}, the discharge capacity returned to 1096 mAh g^{-1}, which indicated a very stable and high-rate cyclic performance.

1. Introduction

Rechargeable lithium ion batteries (LIBs) have been established in the foremost position as universal power sources for portable energy storage systems owing to their high gravimetric and volumetric capacity, high energy density, long cycle life, and relatively low self-discharge [1]. Generally, graphitic materials are commercially used as anode materials in LIB because of structural stability during cycling and flat potential profile versus lithium. However, since graphite as an anode material in LIBs has a theoretical limit of the specific capacity (372 mAh g^{-1}) due to restacking effect [2], prospective further studies to develop new anode materials and structures for the next-generation LIBs, more specifically having high energy density, long life cycle, cost-effectiveness, and environment-friendliness, still remain as a challenging issue [3].

Nanostructured transition metal oxides (TMOs) have been considered as potential anode materials for LIBs because of their diverse merits, such as high reversible capacity, excellent safety, and long cycle life [4,5]. Among them, Fe_3O_4 and Fe_2O_3 have attracted much attention due to their excellent characteristics such as nontoxicity, high theoretical specific capacity ($\approx$1000 mAh g^{-1}), natural abundance, low cost, and environmental friendliness [6]. However, Fe_3O_4 and Fe_2O_3 particles having low intrinsic electrical conductivity and strong agglomeration during the charge and discharge processes show rapid capacity fading owing to large volume changes [7] and subsequent particle pulverization [8]. Therefore, an optimized carbon matrix should be added to get both high electrical conductive and mechanical robustness for reducing volume changes and maximizing the structural stability of the electrodes [9].

Graphene, a single-layer of sp^2 carbon lattices, with excellent charge carrier mobility, mechanical robustness, high thermal conductivity, and chemical stability, has been recognized as one of the

* Corresponding author.
E-mail address: ikoh@kaist.ac.kr (I.-K. Oh).

http://dx.doi.org/10.1016/j.carbon.2017.04.031
0008-6223/

most common carbon matrices for TMO particles to enhance buffering capability for reducing electrode pulverization [4,8,10,11]. Interestingly, Fe_3O_4/graphene systems [8,12] are found to exhibit significant LIB performances owing to the different morphology, porosity of nanostructured electrode materials, which can lead to promote the electrochemical process and preserve the good structural integrity. Furthermore, the assembly of 2D graphene sheets into 3D architecture [13] can make graphene-based composites with fast electron transport pathway, and robust mechanical strength due to the synergy effects of the 3D interconnected framework and the fascinating properties of graphene compared to 2D carbon matrix [14]. Mechanically stable and thermally cross-linked reduced graphene oxide aerogels [15], chemically converted graphene aerogel with superior electrical conductivity [16,17], 3D hierarchical porous N-doped carbon aerogel for supercapacitor electrodes [18], and multifunctional carbon aerogel [19], and steam activated porous graphene aerogel [20] have been recently investigated. Based on the structural features of graphene oxide based aerogels, it can be considered as an ideal prototype for the development of high-performance anode materials for LIBs [21]. Furthermore, different hybrid aerogel structures, such as hybrid of iron nitride and nitrogen-doped graphene aerogel [22], MoS2/graphene aerogels [23], carbon nanotube-bonded graphene hybrid aerogels [24], iron oxide aerogels [25], phase-controlled iron oxide nanobox deposited on hierarchically structured graphene networks [26] have been introduced as anodes for LIBs. In addition, several graphene and polymer based composite aerogels with significant mechanical robustness and electrical conductivity have been also investigated [27].

Moreover, chemical doping is an efficient approach to tailor the electronic properties of graphene and thereby offers very significant impact in energy storage devices [28–31]. Extensive research has revealed that nitrogen doping is effective among various heteroatom doping in graphene owing to its higher electronegativity ($\chi = 3.04$) compared to C ($\chi = 2.55$), which could generate polarization in the sp^2 carbon network, thereby increases the electrical conductivity, electron transfer rate and produces active sites in the graphite lattice for Li ion storage to further promote the electrochemical performance of the electrode. For instance, Wang et al. doped graphene nanosheets with around 2% nitrogen and observed a drastic improvement in the capacity and rate capability of a LIB [29].

However, the main criticism of the graphene-based hybrids and aerogels as anode in LIBs was that large-area graphene sheets protect the fast transport of lithium ions through the thickness direction of the 2D graphene during charge and discharge processes, resulting in a long pathway of lithium ions. This long pathway limits the speed at which the Li-ions can travel during the electrochemical cycling processes. Therefore, a nanohole-structured N-doped 3D graphene framework can be chosen as novel nanostructured anode materials due to their fast and continuous pathway for ion and electron transports. Furthermore, inspired by the synergistic effects of holey graphene, N-doping and TMO nanoparticles, gelatin that is a denatured biopolymer with sufficient N contents can be used for an effective green strategy for the formation of cost-effective and ecofriendly composite anode networked structures, based on gelatin-functionalized and holey graphene oxide. It can be expected that chemical cross-linking would be possible between gelatin chains and functional groups of GO to form a 3D network (Fig. S1 and Fig. S2). The presence of gelatin on graphitic materials is advantageous to form more compact and thinner passive film compare to bare graphene [32]. Furthermore, the mixture of gelatin and graphene oxide during microwave irradiation can be partially transformed to a nitrogen-doped (N-doped) graphene, which can greatly enhance the electrochemical reactivity and electronic conductivity, eventually resulting in superior electrochemical anode performance [33–35]. To the best of our knowledge, a study on nanohole-structured, iron oxide-decorated and N-doped graphene as anode materials for LIBs has not yet been reported.

In this study, we have developed a fast and facile two-step microwave method to synthesize a novel D-N-GG nanostructure consisting of nanoholes and iron oxide particles on N-doped graphene. The resulting D-N-GG nanostructure, which demonstrates a 3D interconnected macroporous structure with a uniform decoration of iron oxide particles on nanohole-structured GG, forms highly conductive networks and short diffusion lengths for lithium ion transport, resulting in a high-rate and high- capacity anode electrode. Furthermore, the D-N-GG structure contains pyridic N and pyrrolic N in N-doped graphene surfaces, as a result of the carbonization of gelatin using microwave irradiation, which improves electrical conductivity, current density as well as the stability of cycle performance. Consequently, the obtained D-N-GG nanostructure exhibited remarkably high-rate capability and specific capacity as the anode electrode in lithium ion battery.

2. Experimental

2.1. D-N-GG nanostructure

For the first microwave step, the GG was dispersed in acetonitrile and 0.5 g of iron acetylacetonate were added and ultrasonicated for 20 min. To generate nanoholes on the surface of gelatin-functionalized graphene (GG), this mixture was subjected to microwave irradiation in microwave ovens (KR-H20MT, Daewoo Electronics Co. Ltd., Korea and MAS-2 Microwave reactor, China) at 700 W for 120 s and 900 W, respectively. In the second microwave step, for decorating iron nanoparticle on the surfaces of nanohole-structured and gelatin-functionalized graphene (N-GG), the N-GG was dispersed again in acetonitrile and 0.2 g of ferrocene and 0.02 g of ADC were added and ultrasonicated for 20 min. Subsequent microwave irradiations were performed again for each 30s.

2.2. Gelatin-functionalized graphene oxide (GG)

Graphene oxide (GO) was prepared from natural graphite powder using modified Hummer's method [36]. For the preparation of gelatin-functionalized graphene oxide, initially, 10 mL (5 mg mL^{-1}) of GO aqueous solution was prepared by ultrasonication followed by slowly addition of 100 mg gelatin to the GO solution. After stirring for 12 h at 50 °C, the resulting mixture dispersion was cooled to room temperature for 10 h. The as-obtained gelatin-functionalized graphene oxide hydrogel was repeatedly washed with cold water to remove unreacted gelatin followed by keeping in the refrigerator for one day. After that, gelatin-functionalized graphene oxide hydrogel was freeze dried for two days to remove the water entrapped in the hydrogel to form spongy gelatin-functionalized graphene oxide.

2.3. Measurements

SEM micrographs were recorded using a Nova NanoSEM 230 FEI at 1 kV in gentle-beam mode without any metal coating. TEM micrographs were recorded on a JEM-3011 HR microscope using a holey-carbon-coated copper grid. For TEM studies, a drop of very dilute dispersion after settling was placed on respective substrates and dried under ambient conditions. Raman spectra were recorded on a LabRAM HR UV/vis/NIR (Horiba JobinYvon, France) using a CW Ar-ion laser (514.5 nm) as an excitation source focused through a confocal microscope (BXFM, Olympus, Japan) equipped with an

objective lens (50×, numerical aperture = 0.50). High-resolution X-ray photoelectron spectroscopy was carried out with a Multilab 2000 system (VG, UK) spectrometer using non-monochromatic Mg Kα X-ray sources. The XPS spectra were curve-fitted with a mixed Gaussian–Lorentzian shape using the XPS peak analysis software, PEAK.

2.4. Anode performance test

The electrode for lithium ion coin cells was prepared by mixing accurately weight of active materials (~72 wt %, 5 mg) along with ketjen black as a conducting additive (KB, ~14 wt %, 1 mg), and Teflonized acetylene black (TAB, ~14 wt %, 1 mg) as a binder. The materials finally pressed on 200 mm^2 stainless steel mesh used as anode and subsequently dried at 160 °C for 4 h in a vacuum oven. The CR2032 coin-type test cells are fabricated in an argon-filled glove box, the anodes are coupled with lithium foil act as both counter and reference electrode and separated by polypropylene separator (Celgard 3401) in 1 M LiPF6 in an ethylene carbonate (EC)/dimethyl carbonate (DMC) (1:1 by v/v., Techno Semichem Co., Ltd, Korea) mixture. The cyclic voltammetry and electrochemical impedance of cells are measured in a Bio-Logic electrochemical work station (SP-150, Biologic, France). The electrochemical cycling tests are performed in a computer-controlled multi-channel battery tester (WBCS 3000, Won-A-Tech, Korea).

3. Results and discussion

3.1. Synthesis and mechanism

The microwave-based self-assembly process for the synthesis of the nanohole-structured, iron oxide-decorated and gelatin-functionalized graphene (D-N-GG) is illustrated in Fig. 1, Figs. S1–S3. The graphite oxide (GO) was synthesized from natural graphite powder by following a modified Hummers method.34 After that, gelatin-functionalized graphene oxide (GG) was made from the mixture of gelatin powder and GO using hydrothermal sol-gel transition method as shown in Fig. S1. There are reactions of abundant functional groups of GO like carboxyl, epoxy groups with $-NH_2$ of gelatin via amide formation and ring opening reaction of epoxy groups of gelatin in GG, as depicted schematically in Fig. S2. The GG was dispersed in acetonitrile and subsequently iron acetylacetonate [$Fe(C_5H_7O_2)_3$] were added and ultrasonicated. This mixture was subjected to microwave irradiation in a microwave reactor to generate nanoholes on the surface of GG. During microwave irradiation, iron acetylacetonate decomposed into Fe_2O_3 and Fe_3O_4 and started to agglomerate on GG surfaces through attachment of oxygen containing groups. However, as microwave irradiation was running for long time with high power about 900 W, agglomerated iron oxides with larger diameter (80–100 nm) penetrated into few-layered GG along the C-axis influencing by the high-temperature at a time. As a result, the big iron oxides formed nanoholes on GG (N-GG) as depicted in Fig. 1a. Simultaneously, amide and amine functional groups of GG along with unreacted amine of decomposed gelatin releasing ammonia. Ammonia can react with the oxygenated functional groups of GG at the edges and in the planar surfaces of GG to form pyrrolic N, pyridinic N and pyridinic N-oxide in GG as shown in Fig. S3a. In the second microwave step, for decorating iron oxide nanoparticle on the surfaces of nanohole-structured GG (N-GG), the N-GG was again dispersed in acetonitrile with ferrocene [$Fe(C_5H_5)_2$] and azodicarbonamide (ADC). Under microwave irradiation with lower power (700 W), as shown in Fig. 1a, several processes occur during the synthesis of the D-N-GG heterostructure. First, the N–GG is to further expand along thickness direction to form the layered and partially exfoliated N-GG due to the several gaseous by-products generated from the microwave decomposition of ADC. The ADC under the microwave irradiation will be transformed into large amounts of carbon dioxide and nitrogen gas, resulting in further expansion along the C-axis of the N-GG. Second is the formation of urea as a by-product of ADC decomposition; urea further reacts by using its amine groups with remaining oxygen moieties, such as carbonyl, carboxyl, and hydroxyl groups of the N-GG to form further N-doping in the graphene surfaces. Third is to separately form iron nanoparticles as catalysts and to release hydrocarbon molecules via the decomposition of ferrocene under microwave irradiation. The decomposed iron nanoparticles are anchored on the oxygenated functional groups of the N-GG, as shown in Fig. 1a and Fig. S3b.

In order to investigate the potential application of the D-N-GG nanostructure as an anode material for lithium ion batteries, galvanostatic charge-discharge studies were carried out as depicted schematically in Fig. 1b. In a conventional Li-ion battery, the cathode electrodes are typically inorganic compounds, such as transition metal oxides, characterized by layered or tunneled structures. The extracted lithium ions from the lithium metal oxide cathodes are moving into a graphitic carbon anode during the charge process. In the discharge cycle, lithium ions inserted into the carbon layers can be readily extracted and transported back to the cathode. Fig. 1b shows that the ideal crystal structure of layered $LiMO_2$ (M = Co, Ni) has a close-packed oxygen array which is slightly distorted from ideal cubic close packing. In our anode electrode system, we expect that the reduction of Fe^{2+} or Fe^{3+} ions to metallic Fe^0 and the formation of amorphous Li_2O will occur during the charging process. Large amounts of Li ions can therefore be stored and released in the Fe_2O_3 or Fe_3O_4 structure through the formation and decomposition of Li_2O respectively, accompanied by the redox reaction of metallic iron during the anodic process.

Especially, the D-N-GG composite electrode has an excellent rate capability with high anode capacity due to the synergistic effects among holey grapheme, gelatin-functionalization, decoration of iron oxide, and 3D interconnected porous conductive framework as follows: 1) accessing more electrolytes and significantly reducing the diffusion length of lithium ions through physical nanoholes, 2) making multidimensional conductive pathways for electron transport form 3D conductive frameworks of D-N-GG, 3) suppressing the particle aggregation and volume expansion by the encapsulation of graphene sheet, 4) providing more active sites for Li storage by N doped surface from gelatin, and 5) binding the graphitic particles with gelatin.

3.2. Morphological analysis

In order to characterize the morphology changes of the carbon nanostructure during the synthesis process, SEM and TEM images of the GG, N-GG, and D-N-GG nanostructures are provided in Fig. 2. The structure of gelatin-functionalized graphene oxide (GG) is shown in Fig. 2a and Fig. S4. The microstructures exhibit randomly oriented porous structures and the presence of the fibrous gelatin chains. During microwave irradiation in the first step, the decomposed iron nanoparticles agglomerate with oxygenated functional groups of the GG surface and then the heated bigger iron nanoparticles produce nanoholes on the graphene surfaces after the additional microwave radiation with much higher power (900 W). And, the heated and agglomerated big iron particles having mechanical kinetic and thermal energies penetrate into few-layered GG along the C-axis. As a result, the big iron nanoparticles with larger diameter (50–100 nm) generate nanoholes on the GG and are embedded into the GG (N-GG) as shown in Fig. 2b. The physical nanoholes with a diameter of 50–100 nm will play a key role in an

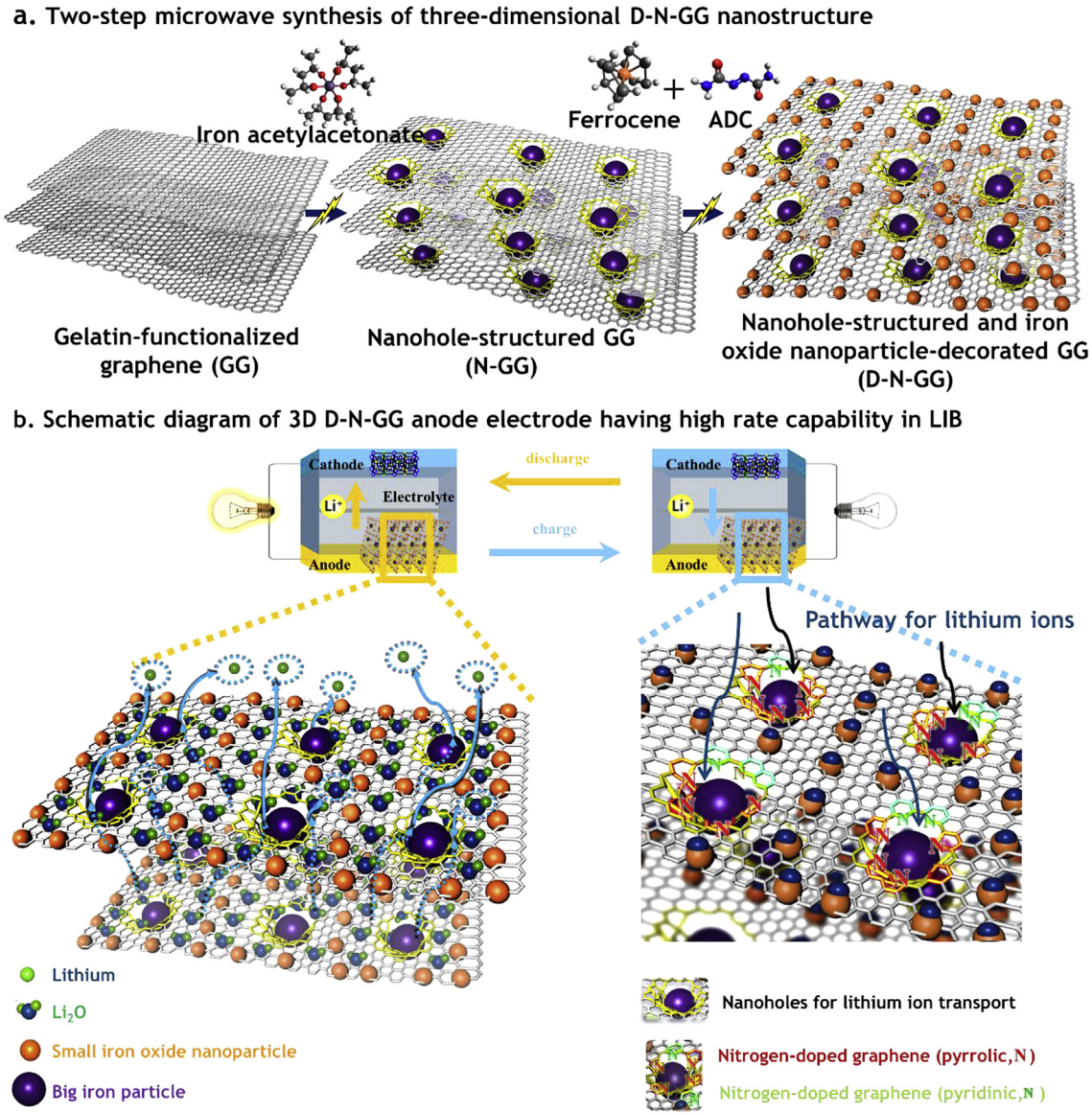

Fig. 1. Two-step synthesis of D-N-GG nanostructure and its application to anode material in lithium ion battery. (a) Step 1, microwave reaction for generating nanohole on the sulfate of gelatin functionalized graphene (N-GG) and Step 2, iron nanoparticle decoration on N-GG. (b) Schematic diagram for charge and discharge in D-N-GG anode material. (A colour version of this figure can be viewed online.)

efficient path way and short diffusion lengths of lithium ions along C-axis of the layered graphene during charge and discharge processes, greatly contributing to superior high rate capability of the anode electrode.

After the second microwave step, the N-GG surfaces are decorated by small iron oxide nanoparticles. Fig. 2c and d exhibit the existence of the nanoholes (shown in yellow color) comprising of big iron nanoparticles (shown in purple color) together with homogeneous distribution of small-sized iron oxide nanoparticles (shown in orange color) on the surface of the graphene sheets in D-N-GG. HR-TEM analysis was carried out to further characterize the microstructures, as shown in Fig. 2d. The higher magnification of the HR-TEM image in Fig. 2d (inset) clearly reveals the lattice planes of iron, indicating its crystalline nature. The HR-TEM images of the iron nanoparticles show that the spacing of the lattice fringes is 0.29 nm, which corresponds to the Fe crystalline planes.

3.3. Chemical structure analysis

The Raman spectra of GG, N-GG, and D-N-GG are shown in Fig. 3a. In the case of a pure graphene, the characteristic G band due to the emission of zone-centered optical phonons is detected at ~1580 cm^{-1} and the disorder-induced D mode is observed at ~1350 cm^{-1}. The G bands for GG, N-GG, and D-N-GG are detected at 1600 cm^{-1}, 1606 cm^{-1}, and 1590 cm^{-1} and the peaks corresponding to the D band are observed at 1355 cm^{-1}, 1414 cm^{-1}, and 1373 cm^{-1}, respectively. Compared to GG and N-GG, the D peak is slightly shifted and the intensity of G Peak is dramatically decreased. The intensity ratios (I_D/I_G), which are the measures of the disorder or of defects, as expressed by the sp^3/sp^2 carbon ratios, of GG, N-GG, and D-N-GG, were 0.99, 1.23, and 1.19, respectively. The intensity ratios of D-N-GG and N-GG is slightly higher than that of GG. The increase of intensity ratio indicates that physical nanoholes produced on the graphene surfaces increase the value of D peak.

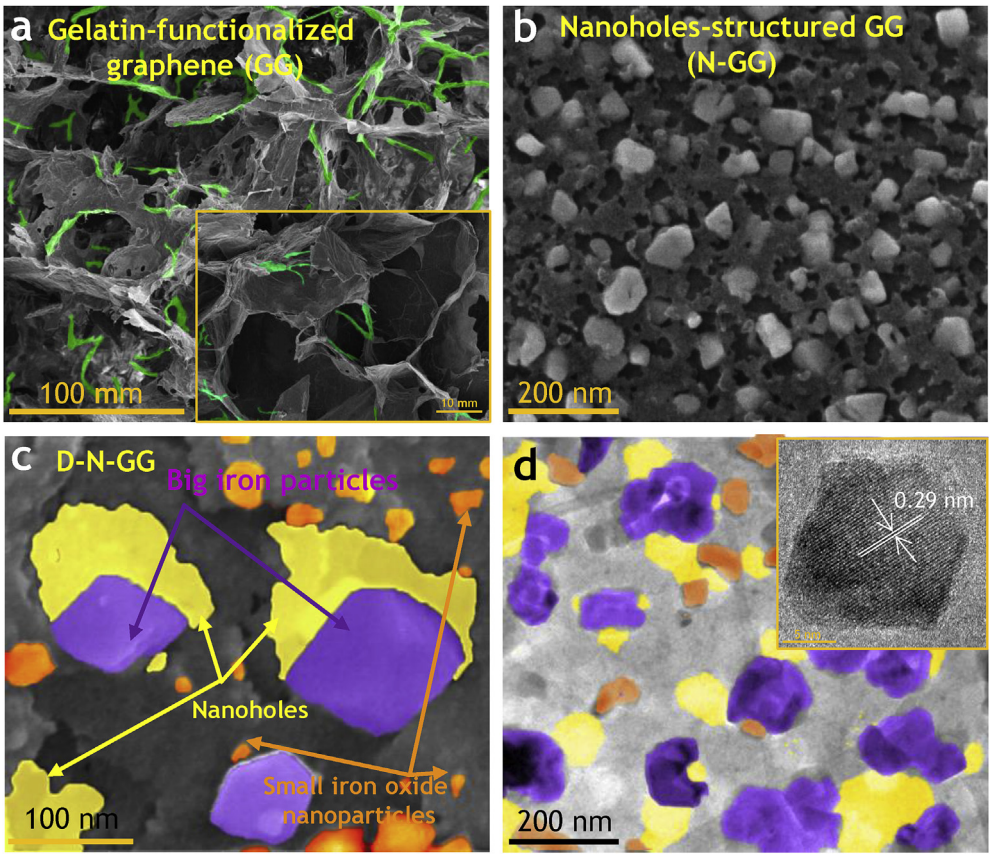

Fig. 2. Morphology of gelatin functionalized graphene (GG) and generation of nanohole and decoration of iron oxide on GG (D-N-GG). Scanning electron microscopy (SEM) images of (a) GG, (b) Big iron oxide particles and decorated small iron oxide particle in D-N-GG, Transmission electron microscopy (TEM) images of (c) large scale D-N-GG heterostructure, (d) colored D-N-GG (yellow:nanohole, purple:big iron oxide, orange: small iron oxide). (A colour version of this figure can be viewed online.)

Another impressive finding is the existence of three kinds of iron-oxide peaks in the N-GG and D-N-GG samples. The N-GG shows the hematite peak (α-Fe_2O_3) located at 704.5 cm^{-1}, the maghemite (γ-Fe_2O_3) peaks located at 350.3, and 503.4 cm^{-1}, and the magnetite (Fe_3O_4) peak located at 661.6 cm^{-1}, respectively. The D-N-GG also has the hematite peaks (α-Fe_2O_3) located at 502.1 cm^{-1} and 704.5 cm^{-1}, the maghemite (γ-Fe_2O_3) peak located at 347.7 cm^{-1}, and the magnetite (Fe_3O_4) peak located at 660.3 cm^{-1}, respectively. Therefore, The Raman spectra imply that the three kinds of iron oxide nanoparticles exist in the N-GG and D-N-GG.

In order to verify the structural changes from GO to D-N-GG, FTIR spectra were investigated. GO shows various kind of oxygenated functional groups. When GO reacted with gelatin, the peak related to −C═O disappeared through amide formation by the reaction of −COOH of GO with $-NH_2$ of gelatin in GG as confirmed by the presence of stretching of amide-I at 1641 cm^{-1}, amide-II at 1542 cm^{-1}, amide-III at 1229 cm^{-1} and amide-VI at 610 cm^{-1}, respectively as depicted in Fig. 3b [37]. Also, the ring opening of epoxy groups of GO took place by gelatin as confirmed by the appearance of C−NH bending (1430 cm^{-1}) and −NH stretching (3290 cm^{-1}) in GG. Interestingly, those aforementioned peaks associated with gelatin functionalization disappeared and concurrently the peaks for C−N stretching at 1145 cm^{-1} appeared in N-GG and D-N-GG indicating formation of efficient N-doping after microwave irradiation. Additionally, the absorption of Fe−O at 580 cm^{-1} in N-GG indicates the big iron nanoparticle, which generates the nanoholes on GG by the 1st step microwave irradiation [38]. And the absorption bands of the oxygen functionalities of GG mostly disappear in N-GG [39]. Interestingly, after the 2nd step microwave irradiation, the hydroxyl group (−OH) was almost reduced in D-N-GG. Furthermore, the Fe−O absorption peaks of hematite at 630 cm^{-1} and 560 cm^{-1} were more intense upon 2nd step of microwave irradiation, suggesting the decoration of small iron nanoparticles on N-GG.

Fig. 3c shows the XRD patterns of GG, N-GG, and D-N-GG. For GG, the peak at $2\theta = 10.92°$ (d = 8.08 Å) [40] indicates that the presence of GO stacking is unaltered even after functionalization with gelatin. The broad peak at $2\theta = 20.0°$(d = 4.4 Å) is attributed to the presence of both gelatin [41] and functionalized graphene oxide. The XRD pattern of N-GG is associated with the magnetite (Fe_3O_4) peaks at $2\theta = 30.24°$ and $2\theta = 43.27°$, the maghemite (γ-Fe_2O_3) peaks at $2\theta = 35.6°$, $2\theta = 53.71°$, $2\theta = 57.25°$, and $2\theta = 62.88°$, and the hematite (α-Fe_2O_3) peak at $2\theta = 35.6°$. In case of the D-N-GG, the magnetite (Fe_3O_4) peak observed at $2\theta = 30.2°$, the maghemite (γ-Fe_2O_3) peaks located at $2\theta = 43.26°$, $2\theta = 57.23°$, and $2\theta = 63.98°$, and the hematite (α-Fe_2O_3) peaks situated at $2\theta = 24.1°$, $2\theta = 33.12°$, $2\theta = 35.59°$, $2\theta = 43.26°$, $2\theta = 57.23°$ and $2\theta = 62.86°$. These results are consistent with the XRD pattern of hematite (JCPDS no. 33-0664), maghemite (JCPDS no. 39-1346), and magnetite (JCPDS no. 65-0731). As the elevated temperature of iron oxide increases under the repeated microwave irradiation, the Fe_3O_4 phase was transformed into Fe_2O_3 phase as documented in the literature [42].

$$Fe_3O_4 \underset{>200°C}{\Rightarrow} \gamma - Fe_2O_3 \underset{>400°C}{\Rightarrow} \alpha - Fe_2O_3$$

Therefore, Fe_2O_3 peaks appear in the D-N-GG more than in the

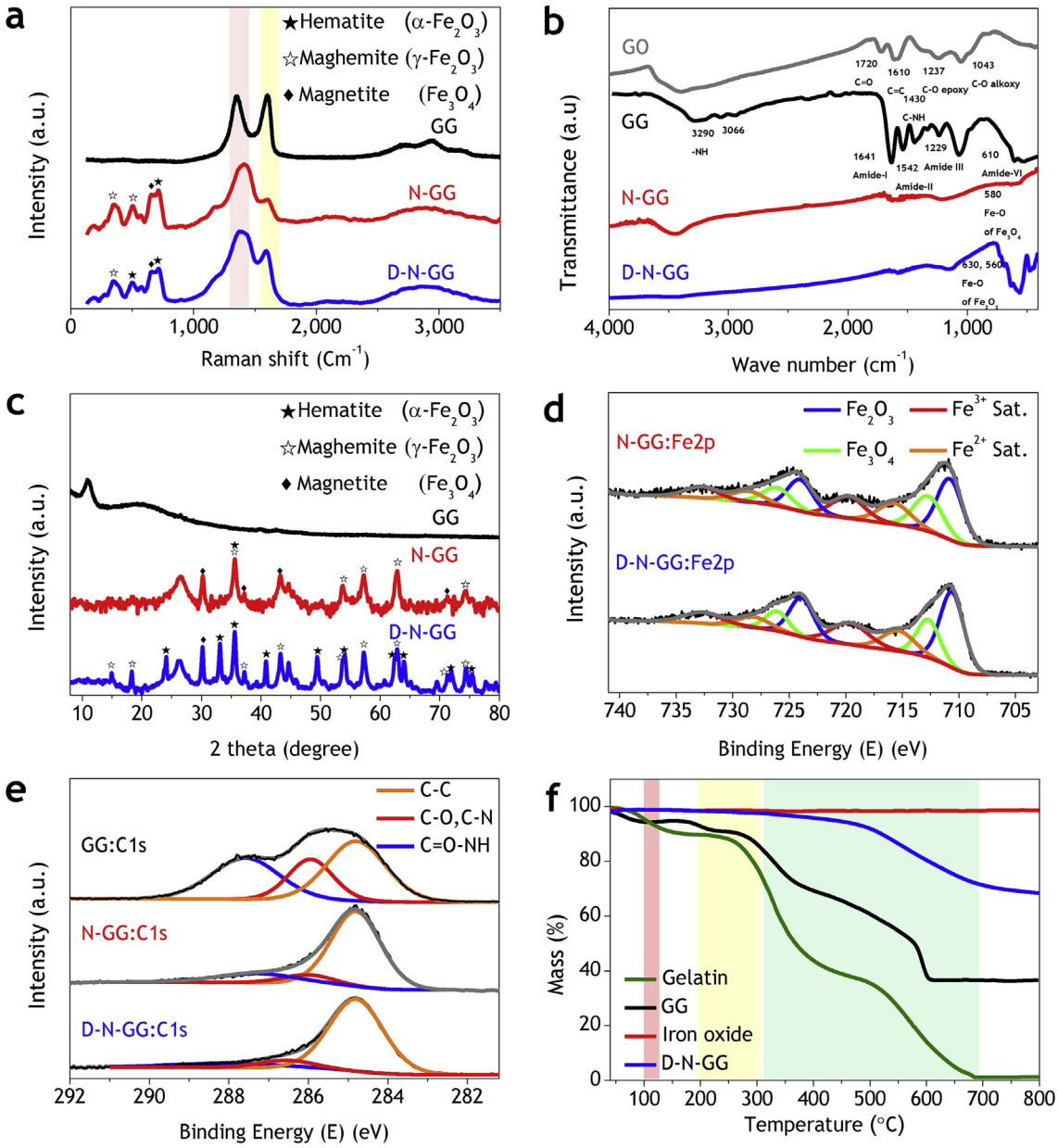

Fig. 3. Chemical structure of 3D carbon nanostructures (GG, N-GG, and D-N-GG). (a) Raman spectra, (b) FT-IR spectra, (c) XRD patterns, deconvoluted Fe2p (d) and C1s (e) XPS spectra of iron, (f) Thermogravimetric analysis. (A colour version of this figure can be viewed online.)

N-GG as shown in Fig. 3c.

The binding state and the quantitative chemical composition of GG, N-GG and D-N-GG were further investigated by X-ray photoelectron spectroscopy (XPS). The existence of N1s in GG infers the successful amide functionalization of GG. And the spectra of N1s and Fe 2p in both N-GG and D-N-GG along with C1s and O1s indicate N-doping through the decomposition of gelatin by microwave irradiation together with nanohole formation and iron oxide decoration in N-GG and D-N-GG.

It is well kwon that C1s peak of GO is deconvoluted into four sub-peaks: C–C (284.8 eV), C–OH or C–O–C (286 eV), C=O (287.0 eV) and –COOH (289.7 eV) [43,44]. After the functionalization of GO with gelatin in GG, the peak corresponding to –COOH vanishes and amide (–CONH) peak appears at 287.58 eV as shown in Fig. 3e. The functionalization is further been reaffirmed by the deconvolution of N1s XPS spectra of GG, which exhibits –CONH peak at 400.5 eV and –NH (or unreacted $-NH_2$ of gelatin) at 400 eV as depicted in Fig. S5d. During the nanohole formation in N-GG by irradiation, the atomic percentage of nitrogen is reduced from 12.33 (GG) to 3.18 and simultaneously iron appears (4.47%). Interestingly, the deconvoluted N1s XPS spectra of N-GG as shown in Fig. S5e indicate the presence of three forms of nitrogen: pyrrolic N and amide N (400.8 eV), pyridinic N (398.6 eV) and pyridinic oxide N (403 eV), all of which have been served as active sites due to N-doping to facilitate nanohole formation of iron oxide in N-GG. In addition, the intensities of amide peak (287.31 eV) and –C–NH or C–OH (286 eV) are significantly reduced due to the decomposition of functional groups through microwave irradiation as shown in Fig. 3e. Further, Fe2p deconvolution exhibits the presence of Fe2p3/2 for Fe_2O_3 (less hematite and more maghemite) at 711.1 eV, Fe2p3/2 for Fe_3O_4 at 712.9 eV and two satellite peaks for Fe^{3+} and Fe^{2+} at 719.8 eV and 715.8 eV, respectively [45]. Furthermore, the existence

of iron oxide at 530.25 eV for O1s deconvolution spectra of N-GG as depicted in Fig. S5b suggests the successful nanohole formation by using heated big iron particles in N-GG.

Similar to N-GG, D-N-GG shows the presence of Fe2p3/2 for Fe_2O_3 (both hematite and maghemite) at 710.6 eV, Fe2p3/2 for Fe_3O_4 at 712.8 eV with much higher intensity than N-GG as shown in Fig. 3d. In particular, the intensity of Fe_2O_3 in D-N-GG is much higher than that of Fe_2O_3 in N-GG due to the phase transition of iron oxide [42]. Theses transformations are irreversible under ambient conditions and have been well studied. Moreover, D-N-GG contains iron oxide more than N-GG by adding ferrocene to N-GG as 2nd metallic catalyst and decorating it as iron oxides on the graphene surfaces of N-GG. As a result, the intensity of iron oxide nanoparticles in D-N-GG increased compared with that in N-GG, as depicted by Fig. S5b and S5c in harmony with XRD and FTIR results. Especially, in D-N-GG, the amide peak for C1s and oxygenated functional groups are almost reduced due to the repeated irradiation as shown in Fig. 3e. And there is the formation of N-doping by the appearance of pyrrolic-N (399.8 eV), pyridinic N (398.6 eV) and pyridinic N-oxide (403 eV) as depicted in Fig. S5f.

TGA was used to determine the composition ratio of each content of gelatin, iron oxide, GG and D-N-GG as shown in Fig. 3f. All the materials show a little mass loss around 100 °C due to the moisture present on the surface. It is well known that GO is thermally unstable and suffers a weight loss around 200–300 °C due to the decomposition of oxygen-containing groups [46]. And gelatin exhibits weight losses in the region of 300 °C–680 °C. Therefore, the main mass loss is ascribed to the two parts in GG: 200–300 °C (due to the decomposition of labile oxygen functional groups) and 300–610 °C (due to the pyrolysis of functionalized gelatin chains with GO). Meanwhile, iron oxide is almost unchanged until 800 °C in the TGA response. In D-N-GG case, there is no dramatic changes in weight loss between 200 and 300 °C as the functional group on GG was already removed by the 2nd step microwave radiations. There are two decomposition steps: 300 °C–610 °C (due to the pyrolysis of carbon structure of GG and gelatin), and 610 °C–680 °C (due to the additional decomposition of gelatin). Therefore, the iron oxide nanoparticles in the D-N-GG are approximately 30 wt%, calculated from the weight residue of GG and D-N-GG.

Porous features of GG and D-N-GG were investigated by N_2 adsorption-desorption isotherm measurements as presented in Fig. S6. Fig. S6 shows IV type isotherms with distinct hysteresis loop at a relative pressure P/P_0 ranging from 0.43 to 1 signifying the existence of mesoporous features (size> 2–50 nm). The calculated Brunauer-Emmett-Teller (BET) surface area of D-N-GG is 25.80 $m^2\ g^{-1}$, higher than that of GG (4.53 $m^2\ g^{-1}$). The average pore width of the D-N-GG and GG are 12.13 and 5.08 nm, respectively. The increase of average pore width and BET value is due to the creation of nanoholes inside the GG layers as a result of the perforation of the GG by the big iron oxide nanoparticles along the C-axis and the decoration of small iron oxide nanoparticles into the GG layers.

3.4. Electrochemical analysis

The Galvanostatic charge and discharge measurement of D-N-GG, N-GG and GG were carried out within the voltage range of 0–3 V at the current rate of 100 mA g^{-1} shown in Fig. 4a. The first cycle discharge capacities of D-N-GG, N-GG and GG are ~2518, 1199 and 461 mAh g^{-1} and the charge capacities are ~1106, 554 and 102 mAh g^{-1}, respectively. The first cycle capacity of D-N-GG from the complete reduction of iron oxide [Fe_xO_y (x,y = 2,3,4)] to iron (Fe) and the solid-electrolyte interface (SEI) layer formation are observed. The lithium ion insertion profile could be divided into three stages. At the early stage (plateau I), a small amount of lithium ions inserted into the iron oxide crystal structure and the hexagonal close packed anionic array are transformed to the cubic stacking structure. During the following stage of lithium insertion (plateau II), a similar profile as plateau I was found. And a long plateau (III) was appeared at approximately 0.79 V, corresponding to the reversible reaction of cubic $Li_2Fe_xO_y$ (x,y = 2,3,4) to Fe. The initial irreversible capacity loss was observed by the formation of the SEI layers below 0.5 V on the electrode surface.

The plateau voltages are clearly reflected from the differential capacity versus voltage plot peaks shown in Fig. 4b. The voltage plateau around ~0.79 V represents the destruction of iron oxide crystal structure by the reduction of iron ions (Fe^{2+} or Fe^{3+}) to the metallic iron (Fe°) and amorphous Li_2O with polymeric gel type SEI layer on the metal nanoparticle surface. On long cycling process, the crystal structure of iron oxide was distracted and the plateaus shifted to the higher potentials ~0.79 V–0.93 V and 1.65 V to 1.92 V for reduction and oxidation peaks observed in the 50th cycle.

To investigate the primary electrochemical performance of D-N-GG, cyclic voltammetry (CV) was analyzed between 0 and 3 V at 0.05 mVs^{-1} scan rate represented in Fig. 4c. The first cycle cathodic scan shows an irreversible peak at ~0.63 V and anodic scan shows a pair of peak at ~1.65 and 1.84 V. The first peak is attributed to the formation of Li_2O species, which result from the conversion reaction of Li^+ intercalation. The latter indicates the redox reaction of iron oxides (Fe_2O_3 and Fe_3O_4) and the formation of SEI layers from the side reaction of electrolytes. In the subsequent CV scan, curves are quite different from that of the first cycle and a pair of reversible peak is shifted more positively to the higher potential [47–50]. According to the CV studies, the possible conversion mechanism was represented in equations (1)–(3),

$$Fe_2O_3 + 2Li^+ + 2e^- \rightarrow Li_2(Fe_2O_3) + 4Li^+ + 4e^- \rightarrow 2Fe^{\circ} + 3Li_2O \quad (1)$$

$$Fe_3O_4 + 2Li^+ + 2e^- \rightarrow Li_2(Fe_3O_4) + 6Li^+ + 6e^- \rightarrow 3Fe^{\circ} + 4Li_2O \quad (2)$$

$$2Fe^{\circ} + 2Li_2O \leftrightarrow 2FeO + 4Li^+ + 4e^- \quad (3)$$

During the charging process, the reduction of Fe^{2+} or Fe^{3+} ions to metallic Fe^0 and the formation of amorphous Li_2O occur. The corresponding discharge process is given as expressed in Eq. (3). It is clear from the above equations that large amount of Li ions can be stored in the iron oxides (Fe_2O_3 and Fe_3O_4) structure through the formation and decomposition of Li_2O accompanied by the redox reaction of metallic iron during the anodic process.

The electrochemical impedance analyses of D-N-GG, N-GG and GG are represented in Fig. 4d. The semicircle at high-medium frequency region for D-N-GG nanostructure was much smaller than the N-GG and GG nanostructures. It can be seen that the solution resistance (R_s) and charge-transfer resistance (R_{ct}) of the D-N-GG nanostructure are 4.44 and 94.038 Ω, respectively, which are significantly lower than those of N-GG (4.62 and 104.5 Ω) and GG (4.74, 186.8 Ω), respectively. The 3D architecture of graphene in D-N-GG can accommodate more electrolytes, significantly improves the conductivity of electrodes and further reduces the charge-transfer resistance at electrode-electrolyte interfaces. The highly conductive path of 3D D-N-GG nanostructure greatly enhances the electrochemical activities of electrode during the long-term cycling.

Fig. 4f shows the cycle profile of D-N-GG, N-GG and GG. Generally, the irreversible reaction leads to electrolyte decomposition, which causes the decrease of the Coulombic efficiency during the first few cycles regarded as a general problem in transition metal oxide anodes. As a results, the columbic efficiencies of three samples were obtained 94, 93 and 78%, respectively at the 1st cycle. At the 40th cycle, the reversible discharge capacities were retained

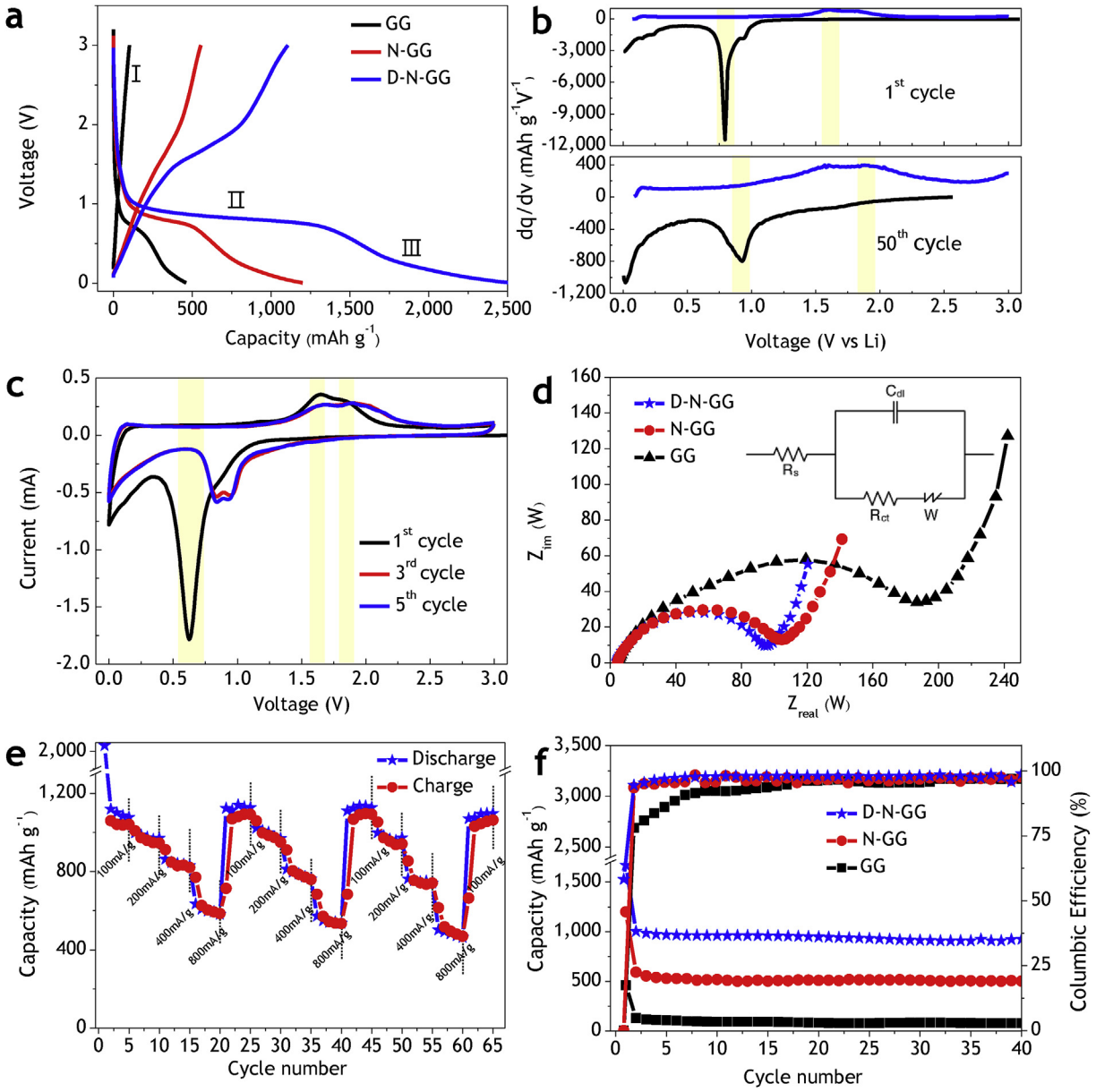

Fig. 4. Anode performances of D-N-GG nanostructure. (a) First discharge curves of a Li^+/D-N-GG cell recorded at current density of 100 mA g^{-1} in potential range of 0–3 V, (b) Differential capacity, (c) C-V response of D-N-GG nanomaterial, (d) Impedance responses of GG, N-GG and D-N-GG, (e) Rate performance, and (f) Specific anode capacity and coulombic efficiency of GG, N-GG and D-N-GG. (A colour version of this figure can be viewed online.)

as high as 924, 503 and 81 mAh g^{-1} with the columbic efficiency are 99, 97 and 96%, respectively. The rate capability of D-N-GG nanostructure measured at different current densities in the range of 100–800 mA g^{-1} from 0 to 3 V depicted in Fig. 4e. The observed discharge capacities were measured as 996, 863 and 634 mAh g^{-1} at the current rates of 200, 400 and 800 mA g^{-1}, respectively. If the current density recovers the original current rate of 100 mA g^{-1} again, the average discharge capacity returns to approximately 1096 mAh g^{-1}, indicating a very stable and high-rate cycle performance.

The D-N-GG composite electrode provides a very high anode capacity with excellent high-rate capability and very stable cyclic stability due to the synergistic effects among the N-doped graphene, iron oxide nanoparticles and three-dimensionally interconnected porous and conductive nanostructures. First, the three-dimensional (3D) nanostructure of D-N-GG provides large surface areas that can access more electrolytes and significantly reduces the diffusion length of lithium ions, resulting in an efficient pathway for fast ion transport. Second, the 3D conductive frameworks of D-N-GG serve as multidimensional conductive pathways for electron transport. Third, the big iron oxide nanoparticles make holey graphene and are embedded into the few-layered graphene, while small iron oxide nanoparticles are decorated on each surface of the graphene sheets. As a result, the porous conductive framework can accommodate volume expansion and suppress the particle aggregation during long cycling. Fourth, 3D carbon nanomaterials with a pyridinic N and a pyrrolic N-doped surface from the gelatin decomposition can provide more active sites for Li storage and facilitate the transfer of Li ions and electrons between the electrodes.

4. Conclusions

In this study, we report a nanohole-structured, iron oxide-decorated and gelatin-functionalized graphene (D-N-GG) for high rate and high capacity Li-ion anode. The obtained D-N-GG nanostructure that was synthesized by multi-step microwave radiations demonstrates 3D interconnected macroporous structure with a uniform decoration of iron oxide particles on nanohole-structured GG, which provides highly conductive networks and short diffusion lengths for lithium ion transport. Furthermore, 3D carbon nanomaterials with N doped surface from gelatin can provide more active sites for Li storage. As a result, the obtained D-N-GG nanostructure exhibits remarkably high anode capacity and excellent rate capability and can be used to meet the high-end requirements of the next-generation lithium ion batteries.

Acknowledgement

This work was partially supported by the Creative Research Initiative Program (2015R1A3A2028975) funded by the National Research Foundation of Korea (NRF).

Appendix A. Supplementary data

Supplementary data related to this article can be found at http://dx.doi.org/10.1016/j.carbon.2017.04.031.

References

[1] D. Liu, G. Cao, Engineering nanostructured electrodes and fabrication of film electrodes for efficient lithium ion intercalation, Energy Environ. Sci. 3 (9) (2010) 1218–1237.
[2] S. Wu, R. Xu, M. Lu, R. Ge, J. Iocozzia, C. Han, B. Jiang, Z. Lin, Graphene-containing nanomaterials for lithium-ion batteries, Adv. Energy Mater 5 (21) (2015) 1500400.
[3] M.M. Thackeray, C. Wolverton, E.D. Isaacs, Electrical energy storage for transportation-approaching the limits of, and going beyond, lithium-ion batteries, Energy Environ. Sci. 5 (7) (2012) 7854–7863.
[4] H. Wang, L.-F. Cui, Y. Yang, H. Sanchez Casalongue, J.T. Robinson, Y. Liang, Y. Cui, H. Dai, Mn_3O_4–graphene hybrid as a high-capacity anode material for lithium ion batteries, J. Am. Chem. Soc. 132 (40) (2010) 13978–13980.
[5] S.-H. Lee, V. Sridhar, J.-H. Jung, K. Karthikeyan, Y.-S. Lee, R. Mukherjee, N. Koratkar, I.-K. Oh, Graphene–nanotube–iron hierarchical nanostructure as lithium ion battery anode, ACS Nano 7 (5) (2013) 4242–4251.
[6] L. Zhang, H.B. Wu, S. Madhavi, H.H. Hng, X.W. Lou, Formation of Fe_2O_3 microboxes with hierarchical shell structures from metal–organic frameworks and their lithium storage properties, J. Am. Chem. Soc. 134 (42) (2012) 17388–17391.
[7] L. Zhang, H.B. Wu, X.W. Lou, Iron-oxide-based advanced anode materials for lithium-ion batteries, Adv. Energy Mater 4 (4) (2014) 1300958.
[8] X. Zhu, Y. Zhu, S. Murali, M.D. Stoller, R.S. Ruoff, Nanostructured reduced graphene oxide/Fe_2O_3 composite as a high-performance anode material for lithium ion batteries, ACS Nano 5 (4) (2011) 3333–3338.
[9] Y. Su, S. Li, D. Wu, F. Zhang, H. Liang, P. Gao, C. Cheng, X. Feng, Two-dimensional carbon-coated graphene/metal oxide hybrids for enhanced lithium storage, ACS Nano 6 (9) (2012) 8349–8356.
[10] D. Wu, F. Zhang, H. Liang, X. Feng, Nanocomposites and macroscopic materials: assembly of chemically modified graphene sheets, Chem. Soc. Rev. 41 (18) (2012) 6160–6177.
[11] Y. Wu, Y. Wei, J. Wang, K. Jiang, S. Fan, Conformal Fe_3O_4 sheath on aligned carbon nanotube scaffolds as high-performance anodes for lithium ion batteries, Nano Lett. 13 (2) (2013) 818–823.
[12] S.-H. Lee, J.-H. Jung, I.-K. Oh, 3D networked graphene-ferromagnetic hybrids for fast shape memory polymers with enhanced mechanical stiffness and thermal conductivity, Small 10 (19) (2014) 3880–3886.
[13] W. Chen, S. Li, C. Chen, L. Yan, Self-assembly and embedding of nanoparticles by in Situ reduced graphene for preparation of a 3D graphene/nanoparticle aerogel, Adv. Mater 23 (47) (2011) 5679–5683.
[14] Z.-S. Wu, Y. Sun, Y.-Z. Tan, S. Yang, X. Feng, K. Müllen, Three-dimensional graphene-based macro- and mesoporous frameworks for high-performance electrochemical capacitive energy storage, J. Am. Chem. Soc. 134 (48) (2012) 19532–19535.
[15] H. Ha, K. Shanmuganathan, C.J. Ellison, Mechanically stable thermally crosslinked poly(acrylic acid)/reduced graphene oxide aerogels, ACS Appl. Mater. Interfaces 7 (11) (2015) 6220–6229.
[16] M.A. Worsley, P.J. Pauzauskie, T.Y. Olson, J. Biener, J.H. Satcher, T.F. Baumann, Synthesis of graphene aerogel with high electrical conductivity, J. Am. Chem. Soc. 132 (40) (2010) 14067–14069.
[17] J. -Y. Hong, J.J. Wie, Y. Xu, H.S. Park, Chemical modification of graphene aerogels for electrochemical capacitor applications, Phys. Chem. Chem. Phys. 17 (46) (2015) 30946–30962.
[18] Y. Hu, X. Tong, H. Zhuo, L. Zhong, X. Peng, S. Wang, R. Sun, 3D hierarchical porous N-doped carbon aerogel from renewable cellulose: an attractive carbon for high-performance supercapacitor electrodes and CO_2 adsorption, RSC Adv. 6 (19) (2016) 15788–15795.
[19] H. Sun, Z. Xu, C. Gao, Multifunctional, ultra-flyweight, synergistically assembled carbon aerogels, Adv. Mater 25 (18) (2013) 2554–2560.
[20] Z.-Y. Sui, Q.-H. Meng, J.-T. Li, J.-H. Zhu, Y. Cui, B.-H. Han, High surface area porous carbons produced by steam activation of graphene aerogels, J. Mater. Chem. A 2 (25) (2014) 9891–9898.
[21] R. Wang, C. Xu, J. Sun, L. Gao, Three-Dimensional Fe_2O_3 nanocubes/nitrogen-doped graphene aerogels: nucleation mechanism and lithium storage properties, Sci. Rep. 4 (2014) 7171.
[22] H. Yin, C. Zhang, F. Liu, Y. Hou, Hybrid of iron nitride and nitrogen-doped graphene aerogel as synergistic catalyst for oxygen reduction reaction, Adv. Funct. Mater 24 (20) (2014) 2930–2937.
[23] M.A. Worsley, S.J. Shin, M.D. Merrill, J. Lenhardt, A.J. Nelson, L.Y. Woo, A.E. Gash, T.F. Baumann, C.A. Orme, Ultralow density, monolithic WS_2, MoS_2, and MoS_2/graphene aerogels, ACS Nano 9 (5) (2015) 4698–4705.
[24] S. Kabiri, D.N.H. Tran, T. Altalhi, D. Losic, Outstanding adsorption performance of graphene–carbon nanotube aerogels for continuous oil removal, Carbon 80 (2014) 523–533.
[25] J.W. Long, M.S. Logan, C.P. Rhodes, E.E. Carpenter, R.M. Stroud, D.R. Rolison, Nanocrystalline iron oxide aerogels as mesoporous magnetic architectures, J. Am. Chem. Soc. 126 (51) (2004) 16879–16889.
[26] S. Yun, Y.–C. Lee, H.S. Park, Phase-controlled iron oxide nanobox deposited on hierarchically structured graphene networks for lithium ion storage and photocatalysis, Sci. Rep. 6 (2016) 19959.
[27] S. Das, F. Irin, L. Ma, S.K. Bhattacharia, R.C. Hedden, M.J. Green, Rheology and morphology of pristine graphene/polyacrylamide gels, ACS Appl. Mater. Interfaces 5 (17) (2013) 8633–8640.
[28] D. Deng, X. Pan, L. Yu, Y. Cui, Y. Jiang, J. Qi, W.-X. Li, Q. Fu, X. Ma, Q. Xue, G. Sun, X. Bao, Toward n-doped graphene via solvothermal synthesis, Chem. Mater 23 (5) (2011) 1188–1193.
[29] H. Wang, C. Zhang, Z. Liu, L. Wang, P. Han, H. Xu, K. Zhang, S. Dong, J. Yaoa, G. Cui, Nitrogen-doped graphene nanosheets with excellent lithium storage properties, J. Mater. Chem. 21 (14) (2011) 5430–5434.
[30] C. Ma, X. Shao, D. Cao, Nitrogen-doped graphene nanosheets as anode materials for lithium ion batteries: a first-principles study, J. Mater. Chem. 22 (18) (2012) 8911–8915.
[31] X. Wang, X. Li, L. Zhang, Y. Yoon, P.K. Weber, H. Wang, J. Guo, H. Dai, N-doping of graphene through electrothermal reactions with ammonia, Science 324 (5928) (2009) 768–771.
[32] R. Dominko, M. Gaberscek, M. Bele, J. Drofenik, E.M. Skou, A. Würsig, P. Novák, J. Jamnik, Understanding the role of gelatin as a pretreating agent for use in Li-ion batteries, J. Electrochem. Soc. 151 (7) (2004) A1058–A1062.
[33] L. Qie, W.-M. Chen, Z.-H. Wang, Q.-G. Shao, X. Li, L.-X. Yuan, X.-L. Hu, W.-X. Zhang, Y.-H. Huang, Nitrogen-doped porous carbon nanofiber webs as anodes for lithium ion batteries with a superhigh capacity and rate capability, Adv. Mater 24 (15) (2012) 2047–2050.
[34] C. Zhang, N. Mahmood, H. Yin, F. Liu, Y. Hou, Synthesis of phosphorus-doped graphene and its multifunctional applications for oxygen reduction reaction and lithium Ion batteries, Adv. Mater 25 (35) (2013) 4932–4937.
[35] F. Zheng, Y. Yang, Q. Chen, High lithium anodic performance of highly nitrogen-doped porous carbon prepared from a metal-organic framework, Nat. Commun. 5 (2014).
[36] W.S. Hummers, R.E. Offeman, Preparation of graphitic oxide, J. Am. Chem. Soc. 80 (6) (1958), 1339–1339.
[37] D. Du, P. Li, J. Ouyang, Nitrogen-doped reduced graphene oxide prepared by simultaneous thermal reduction and nitrogen doping of graphene oxide in air and its application as an electrocatalyst, ACS Appl. Mater. Interfaces 7 (48) (2015) 26952–26958.
[38] D.N.H. Tran, S. Kabiri, L. Wang, D. Losic, Engineered graphene-nanoparticle aerogel composites for efficient removal of phosphate from water, J. Mater. Chem. A 3 (13) (2015) 6844–6852.
[39] I. Andjelkovic, D.N.H. Tran, S. Kabiri, S. Azari, M. Markovic, D. Losic, Graphene aerogels decorated with α-FeOOH nanoparticles for efficient adsorption of arsenic from contaminated waters, ACS Appl. Mater. Interfaces 7 (18) (2015) 9758–9766.
[40] I.K. Moon, S. Yoon, K.-Y. Chun, J. Oh, Highly elastic and conductive N-doped monolithic graphene aerogels for multifunctional applications, Adv. Funct. Mater 25 (45) (2015) 6976–6984.
[41] A. Bigi, S. Panzavolta, K. Rubini, Relationship between triple-helix content and mechanical properties of gelatin films, Biomaterials 25 (25) (2004) 5675–5680.
[42] A.M. Jubb, H.C. Allen, Vibrational spectroscopic characterization of hematite, maghemite, and magnetite thin films produced by vapor deposition, ACS Appl. Mater. Interfaces 2 (10) (2010) 2804–2812.
[43] M. Kotal, J. Kim, K.J. Kim, I.-K. Oh, Sulfur and nitrogen co-doped graphene electrodes for high-performance ionic artificial muscles, Adv. Mater 28 (8) (2016) 1610–1615.

[44] R. Kumar, J.-H. Oh, H.-J. Kim, J.-H. Jung, C.-H. Jung, W.G. Hong, H.-J. Kim, J.-Y. Park, I.-K. Oh, Nanohole-structured and palladium-embedded 3D porous graphene for ultrahigh hydrogen storage and CO oxidation multifunctionalities, ACS Nano 9 (7) (2015) 7343–7351.
[45] L. Ren, S. Huang, W. Fan, T. Liu, One-step preparation of hierarchical superparamagnetic iron oxide/graphene composites via hydrothermal method, Appl. Surf. Sci. 258 (3) (2011) 1132–1138.
[46] R. Larciprete, P. Lacovig, S. Gardonio, A. Baraldi, S. Lizzit, Atomic oxygen on graphite: chemical characterization and thermal reduction, J. Phys. Chem. C 116 (18) (2012) 9900–9908.
[47] M.V. Reddy, T. Yu, C.H. Sow, Z.X. Shen, C.T. Lim, G.V. Subba Rao, B.V.R. Chowdari, α-Fe_2O_3 nanoflakes as an anode material for Li-ion batteries, Adv. Funct. Mater 17 (15) (2007) 2792–2799.
[48] S.H. Lee, S.-H. Yu, J.E. Lee, A. Jin, D.J. Lee, N. Lee, H. Jo, K. Shin, T.-Y. Ahn, Y.-W. Kim, H. Choe, Y.-E. Sung, T. Hyeon, Self-assembled Fe_3O_4 nanoparticle clusters as high-performance anodes for lithium ion batteries via geometric confinement, Nano Lett. 13 (9) (2013) 4249–4256.
[49] C. He, S. Wu, N. Zhao, C. Shi, E. Liu, J. Li, Carbon-encapsulated Fe_3O_4 nanoparticles as a high-rate lithium ion battery anode material, ACS Nano 7 (5) (2013) 4459–4469.
[50] J. Chen, L. Xu, W. Li, X. Gou, α-Fe2O3 nanotubes in gas sensor and lithium-ion battery applications, Adv. Mater 17 (5) (2005) 582–586.